Heliyon 10 (2024) e32199

Contents lists available at ScienceDirect

Heliyon

journal homepage: www.cell.com/heliyon

Research article

Tracking head movement inside an MR scanner using electromagnetic coils

E.H. Bhuiyan [a,b,*], M.E.H. Chowdhury [a,c,**], P.M. Glover [a]

[a] Sir Peter Mansfield Imaging Centre, School of Physics and Astronomy, University of Nottingham, Nottingham, NG7 2RD, UK
[b] Center for Magnetic Resonance Research, University of Illinois Chicago, Chicago, IL 60612, USA
[c] Electrical Engineering, Qatar University, Doha 2713, Qatar

ARTICLE INFO

Keywords:
Real-time motion tracking
EMF tracking
Head motion
Prospective motoring
Coils array

ABSTRACT

Prospective motion corrections in brain imaging for MRI are fairly challenging. Monitoring involuntary head movement inside MR scanner is crucial for prospective motion correction. This initial study delves into utilizing simulations to track the head's movements within an MRI scanner, achieved by measuring induced voltage changes from time-varying magnetic field gradients in head-mounted coils. The ultimate aim is to create an inventive approach for prospective motion corrections. The voltage induced in a circular coil of wire that is exposed to time-varying x-, y- and z-magnetic field gradients, is calculated for varying positions and orientations (POSE) of the coils. Similar steps are taken for a system of five coils confined to faces of a cube and it is established whether the voltage changes due to gradient pulses applied along three directions can be used to calculate the change in POSE of the set of coils. This induced voltage led to form a system of linear equations and then find a calibration matrix. Inverting the calibration matrix enables the estimation of movement parameters from the calculated voltage in the coils. Our software gives robust measurement of the six degrees of freedoms to monitor head movement accurately so far ≈ 0.3 mm and $\approx 0.05°$. By using this standard method one can identify the POSE of the coils as well head within an MR scanner. Even after, addition of noise voltage (up to 20 μV) estimated parameters does not blow up. This electromagnetic field based real-time tracking is highly accurate, non-invasive and compatible with standard MRI hardware.

1. Introduction

MRI technology has advanced significantly over the last half century, but one of the greatest causes of dissatisfaction in the research community is that movement on the patient's during the procedure obscures the results, and typically results in the MRI needing to be redone. Approximately one in every five MRI scans needs to be repeated due to image quality degradation caused by patient movement, as highlighted in research by Godenschweger [1]. The resulting motion artifacts incur a substantial financial

* Corresponding author at: Center for Magnetic Resonance Research, University of Illinois Chicago, Chicago, IL 60612, USA.
** Corresponding author at: Electrical Engineering, Qatar University, Doha 2713, Qatar.
E-mail addresses: bhuiyan@uic.edu (E.H. Bhuiyan), mchowdhury@qu.edu.qa (M.E.H. Chowdhury).

https://doi.org/10.1016/j.heliyon.2024.e32199
Received 14 March 2023; Received in revised form 4 September 2023; Accepted 29 May 2024

Available online 4 June 2024

burden on the healthcare sector, amounting to over $1 billion annually, as indicated by Pierre [2]. Challenges related to patient motion are particularly pronounced when dealing with non-cooperative patient groups like children or infants [3,4], cases involving trauma or stroke patients [5], individuals affected by agitation due to anxiety or pain, and those with movement disorders such as Parkinson's disease [6], as well as conditions like Alzheimer's disease [7], Huntington's disease [8], and multiple sclerosis [9]. Consequently, there exists a pressing need to develop effective methods for motion correction in clinical MRI.

Motion artefacts are a serious problem in many MRI applications. Small head movements during image acquisition produce artefacts in magnetic resonance images. In functional MRI (fMRI) time series, movement between consecutive acquisitions of the same slice lead to image misregistration which can produce spurious activation in fMRI data. In anatomical MRI, movement between acquisitions of different data segments in k-space (the Fourier domain) generates image artefacts [10]. With additional information about the movement, it is possible to improve the re-alignment of images in fMRI time series and potentially to eliminate the artefacts in anatomical images by re-aligning the k-space data (known as "retrospective" correction). If movement information is recorded and processed during the image acquisition it is possible to adjust the image acquisition geometry [10] in "real time" so that the artefacts are eliminated. This is known as "prospective" motion correction.

Various methods [11–19] have been developed for prospective and retrospective motion correction, and a lot of research has been carried out on this topic in the last two decades. Motion sensitivity is still however an unsolved (have partial solution) problem in MRI, as well as in fMRI. There can be some problems with implementing this method which still need to be solved. For instance, it becomes problematic when any shifting of the object creates changes in the magnetic field leading to changes in image distortion [10]. Several alternative approaches have been devised to monitor head movement within the MRI scanner, as detailed in the studies by Andersen, Lei and colleagues, Wildey, Maclaren and partners, Tobias and others, and Rasmus [20–25]. These methodologies encompass various techniques, including employing optical detection through the line of sight and utilizing compact NMR coils. Furthermore, additional investigations have concentrated on implementing prospective motion correction strategies to address head movements. For instance, one notable approach is the real-time intra-volume motion correction in EPI (Echo Planar Imaging) using active markers, as described by M.B. Ooi et al. [26]. Additionally, there is research by J. Maclaren et al. that focuses on predicting head positions during rapid subject motion in EPI [27]. Another advancement involves real-time slice-by-slice motion correction tailored for fMRI studies involving subjects in unconstrained motion, discussed in the work by O. Speck and colleagues [28]. Notably, Rainer et al. have contributed by introducing a technique that combines both prospective motion correction and distortion correction for EPI [29].

Bhuiyan et al. extensively analyzed the background theory and feasibility of this experimental work using a generalized linear model [30]. Several studies have demonstrated the effectiveness of EMF-based motion tracking in reducing motion artifacts in MRI images. For example, a study by Thesen et al. [31] found that EMF-based motion tracking significantly reduced motion artifacts in functional MRI (fMRI) scans, leading to more accurate data. Another study by Liu et al. [32] showed that EMF-based motion tracking improved the quality of diffusion-weighted MRI (DWI) images, which are sensitive to motion artifacts. Additionally, advancements in deep learning algorithms have also been explored to further enhance the accuracy of motion tracking. For example, a recent study by Heye et al. [33] suggested a deep learning-based motion correction technique that significantly improved the accuracy of fMRI data. Overall, the development of novel and improved motion tracking techniques remains a vibrant area of investigation in the MRI community, with the goal of enabling more accurate and reliable imaging data. Roth and Nevo et al. [35], in their study, showcased a tracking system that harnessed the gradient fields of MRI scanners using a bespoke sequence. This approach was implemented without making any modifications to the scanner's hardware or operational mode, as detailed in their research [35].

Frost and colleagues investigated the application of high-frequency motion correction within imaging echo trains, merging markerless head motion tracking with a neuroanatomical MRI sequence that underwent prospective correction [36]. In a similar vein, Laustsen and associates leveraged electroencephalography (EEG) hardware to monitor head movement. This was achieved by capturing signals induced by inherent imaging gradients and subsequently deducing motion based on the recorded gradient switching patterns [34]. Motion correction in EEG systems is an active area of research to improve the accuracy and reliability of EEG signals, particularly for applications such as brain-computer interfaces and neurofeedback training. Several methods have been developed, including using motion sensors and optical cameras to track head movement, as well as developing algorithms for real-time motion correction. Recent research has also explored the use of deep learning-based techniques for motion correction in EEG systems. As an illustration, Lin et al. [37] conducted research that introduced a method rooted in deep learning. This technique aimed at both eliminating artifacts and rectifying motion-related issues present in EEG signals, resulting in a notable enhancement in the precision of the captured data. Another study by Chen et al. [38] investigated the use of convolutional neural networks for real-time motion correction in EEG signals, demonstrating improved performance compared to existing methods. Overall, motion correction in EEG systems remains an active area of investigation with the objective of enhancing the precision and dependability of EEG signals across various applications. Afacan O. et al. modified the MPRAGE sequence to quantify motion utilizing the EM tracking system at intervals of one repetition time [39]. Other techniques included the use of NMR probes [40], sensors [41], and stripe structure light [42].

All these techniques have some advantages and disadvantages that listed in the Table 1.

This preliminary study proposes using a set of inductive coils woven into a cap placed on the scalp to measure motion. This objective will be achieved through the surveillance of voltages induced within the coils, induced by the dynamic magnetic field gradients administered in the MRI sequence. The alterations in these induced voltages will be linked to shifts in the positioning and alignment of the head. Recording these voltages can be achieved by integrating a Brain Products EEG system with the coils. To evaluate the plausibility of the simulation, a preliminary trial was carried out. The intent behind this trial was to ascertain the simulation's capacity to faithfully emulate the system's responses within distinct conditions.

Table 1
Comparison among the motion tracking techniques.

Technique	Description	Advantages	Disadvantages
Gradient-based	Utilizes the gradient fields of MRI scanners through a custom sequence	Does not require additional hardware or modification of the scanner	Limited to small movements and prone to inaccuracies
EEG-based	Utilizes electroencephalography (EEG) hardware to record signals induced by native imaging gradients	Can accurately detect head motion in real-time	Limited to small movements and may have interference from other signals
EM tracking	Utilizes an electromagnetic (EM) tracking system to measure motion using the MPRAGE sequence	Can provide accurate measurements of head motion	Requires additional hardware and may be prone to electromagnetic interference
Markerless	Utilizes high-frequency movement correction during imaging echo trains to combine markerless head motion with neuroanatomical MRI sequences	Can accurately detect head motion without the need for markers or additional hardware	Limited to small movements and may be prone to inaccuracies
NMR probes	Utilizes nuclear magnetic resonance (NMR) probes to measure motion	Can provide accurate measurements of head motion	Requires additional hardware and may be limited in terms of applicability
Sensor-based	Utilizes sensors to measure head motion	Can provide accurate measurements of head motion	Requires additional hardware and may be limited in terms of applicability
Stripe structure light	Utilizes stripe structure light to track head motion	Can accurately detect head motion in real-time	Requires additional hardware and may be limited in terms of applicability

2. Theory underlying the simulations

The simulations rely on the utilization of Faraday's electromagnetic induction principle. Yet, directly applying this law to compute alterations in induced voltages is not always straightforward, particularly when dealing with conductive materials where defining the pertinent area for flux change can pose challenges. Nevertheless, the induced voltage can be directly determined from the rate of flux change linked through the wire loop, employing the subsequent equation (Eq. (1)) as described in the work by Jackson [44].

$$\begin{aligned} -V &= \frac{\partial}{\partial t}\left(\int_S \mathbf{B}\cdot .d\mathbf{S}\right) = \oint \frac{\partial \mathbf{A}}{\partial t}\cdot \mathbf{dl} \\ &= \oint \left(\frac{\partial \mathbf{A_x}}{\partial t} + \frac{\partial \mathbf{A_y}}{\partial t} + \frac{\partial \mathbf{A_z}}{\partial t}\right)\cdot \mathbf{dl}, \end{aligned} \tag{1}$$

where, the vector potential $\mathbf{A}$ is connected to the magnetic field, $\mathbf{B}$, by $\mathbf{B} = \nabla \times \mathbf{A}$, and the application of Stokes' theorem has been employed to transform the surface integral into a closed-line integral.

Subsequent (Eqs. (2)-(4)) vector potentials [45–48] for the different gradients are used in these simulations.
Longitudinal (z) gradient:

$$\mathbf{A_z} = -\frac{1}{2}G_z yz\hat{i} + \frac{1}{2}G_z xz\hat{j}. \tag{2}$$

Transverse (x) gradient:

$$\mathbf{A_x} = -\frac{1}{2}G_x xy\hat{i} + \frac{1}{4}G_x(x^2 - y^2)\hat{j} + G_x yz\hat{k}. \tag{3}$$

Transverse (y) gradient:

$$\mathbf{A_y} = \frac{1}{4}G_y(x^2 - y^2)\hat{i} + \frac{1}{2}G_y xy\hat{j} - G_y xz\hat{k}, \tag{4}$$

where G is an amplitude of a gradient and the rest of the symbols are conventional.

3. Simulations

This investigation employs simulations to explore the potential of tracking human head movements within an MRI scanner. This is achieved by evaluating alterations in voltages induced within coils mounted on the head, influenced by the inherent gradients of the

MRI scanner. Initially, circular coils are generated within the xy-, yz-, and zx-planes, and the consequential voltage fluctuations are computed as a result of translations and rotations during the application of magnetic field gradients. A similar process is undertaken for a configuration of five coils positioned on the faces of a cube, aimed at determining whether voltage changes resulting from gradient pulses along three directions can be harnessed for deducing alterations in the coils' POSE. Subsequently, a calibration matrix is constructed by fitting the computed coil voltages through a system of linear equations (Ax = V), where A signifies the calibration matrix, x denotes the POSE, and V represents the voltage variations. This established calibration matrix, along with the variations in induced voltage, is then utilized for inferring the parameters associated with movement.

The electromotive force (EMF) generated within a coil due to alterations in its magnetic flux environment can be computed by employing Faraday's law of electromagnetic induction [43]

$$\oint \mathbf{E} \cdot \mathbf{dl} = -\frac{\mathrm{d}}{\mathrm{dt}} \int \mathbf{B} \cdot \hat{\mathbf{n}} \mathrm{da} = -\frac{\mathrm{d}}{\mathrm{dt}} \left(\int_s \mathbf{B} \cdot \mathbf{ds} \right), \tag{5}$$

where **B** represents the magnetic field and **E** is the electric field. By delineating the magnetic flux through a surface to be

$$\phi_B = \int \mathbf{B} \cdot \mathbf{dS} \tag{6}$$

and considering the case where the surface is bounded by a wire loop, the (emf) or voltage induced across the ends of the wire is given by

$$V = \oint \mathbf{E} \cdot \mathbf{dl}. \tag{7}$$

When Eq. (6) and Eq. (7) are substituted into Eq. (5), a more familiar form of Faraday's law (Eq. (8)) is found:

$$V = -\frac{\mathrm{d}\phi_B}{\mathrm{dt}}. \tag{8}$$

Faraday's principle establishes that when there is a fluctuating magnetic flux passing through a loop of wire or any circuit, it gives rise to a voltage whose magnitude is directly proportional to the rate at which the flux changes. The concept of flux can be likened to the quantity of field lines that traverse the effective area encompassed by the loops forming the coils.

In this study, the voltage induced in the circular coils and the change in voltage induced within the coils is calculated due to positional changes. By analyzing the data and comparing the pattern of voltage changes across coils, it is possible to characterize the positional changes and associate the pattern of voltage changes with particular movements.

4. Results

Circular coils are generated in the planes, and the change in induced voltages is calculated due to translation and rotation of the coils during the execution of x-, y-, and z-gradients. Using the calculated induced voltage and their linear fitting, a system of linear equations (Ax = V) is formed. A calibration matrix A is generated from the slopes of the linear fittings. POSE can be estimated by taking the inversion of the calibration matrix ($V = A^{-1}x$).

4.1. The change in induced EMF in a circular coil

Circular coils are generated in the xy-, yz-, and zx-planes as shown in Fig. 1(a), (c) and (e), respectively. The variation in EMFs induced in the coils due to time-varying x-, y-, and z-gradients is calculated for consecutive translations along the x-, y-, and z-axes. Fig. 1(b), (d) and (f) show the linear changes in induced voltage in the coils.

In Fig. 1(a), (c) and (e) C_o stands for centers, L_o stands for the coil wire path before translation and R denotes the radius of the coil. On the other hand, C_{Tx}, C_{Ty} and C_{Tz} stands for centers, L_{Tx}, L_{Ty} and L_{Tz} stands for the coil wire path after 10 mm translation along the x-, y- and z-axes. Fig. 1(b), (d) and (f) shows the gradient induced EMFs changes linearly with consecutive shifts of a coil along the x-, y- and z-axes during the application of x-, y- and z-gradients. After analyzing all the calculated data, it can be concluded that within the range of gradient linearity, the induced voltage in a circular coil varies linearly with position during the execution of x-, y-, and z-gradients for any translation.

Circular coils in the xy-, yz-, and zx-planes are generated and its rotation about the x-, y- and z-axes is shown in Fig. 2(a), (c) and (e). The corresponding change in induced voltage in a coil is linear with respect to rotation about the x-, y- and z-axes during execution of y-, x- and z-gradient for these small angles of rotation as shown in Fig. 2(b), (d) and (f).

In Fig. 2(a), (c) and (e) C_{Rx}, C_{Ry} and C_{Rz} stand for centers, L_{Rx}, L_{Ry} and L_{Rz} stand for the coil wire path after 5° rotation about the x-, y- and z-axes. The voltage changes linearly with respect to rotation angles for these small angles of rotation. The change in induced voltage due to the three types of rotation is thoroughly calculated while implementing gradients along the x-, y-, and z-axes when the coils are in different planes. Due to x- and y-rotation during execution of z-gradient the voltage change is quadratic in a coil for some special orientation even for small angles of rotation. This issue is addressed in detail in sub-subsection 4.4. It is worth noting that linear changes when present dominate over quadratic changes. According to theory and simulation [49] there is no change in the voltage induced in the coils due to rotation about the z-axis.

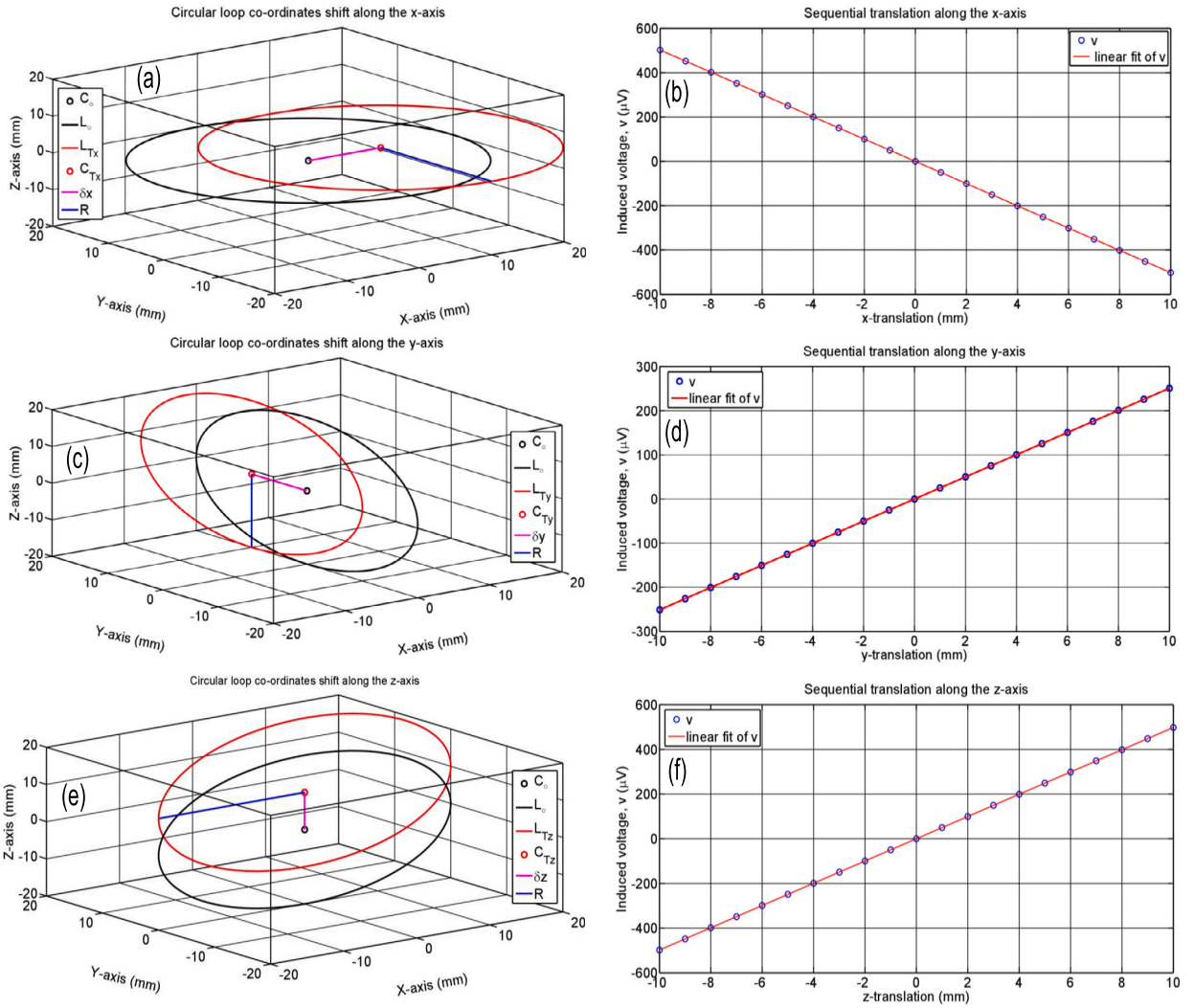

Fig. 1. Translation along the x-, y- and z-axes. (a) A circular coil in the xy-plane having 10 turns shifted 10 mm along the x-axis. (b) Linear changes in induced voltage due to an x-translation during execution of an x-gradient. (c) A circular coil in the yz-plane and shifted 10 mm along the y-axis. (d) Linear changes in induced voltage due to y-translation during execution of a z-gradient. (e) A circular coil in zx-plane and shifted 10 mm along the z-axis. (f) Linear changes in induced voltage due to z-translation during execution of a z-gradient. The change in induced voltage in the coil is linear due to translation along any direction from the magnetic isocenter during the execution of x-, y-, and z-gradients.

4.2. A system of five coils

Exactly the same simulation parameters and 10 turns are used for a single coil, but as the MATLAB code was generalized and restructured for a system of five coils. The coils are located on the faces of a cubic box of side $2r_c$ which is shown in Fig. 3, where $L_1C_1(0,0,r_c)$, $L_2C_2(r_c,0,0)$, $L_3C_3(0,-r_c,0)$, $L_4C_4(0,r_c,0)$, and $L_5C_5(0,-r_c,0)$ are the centers of the respective coils and O is the origin.

The system having five coils in the xy-, yz- and zx-planes is translated 10 mm along the x- y- and z-axes, during execution of x-, y- and z-gradient are shown in Fig. 4(a-c) respectively. The orientation of the coils remains unchanged in this case.

Rotation of the system of five coils about the x-, y- and z-axes is shown in Fig. 5. In this case the coils C_1, C_4 and C_5 change their orientation due to x-rotation as shown in Fig. 5(a), but the coils C_2 and C_3 remain unchanged. Similarly, due to rotation about the y-axis the coils C_1, C_4 and C_5 change their orientation but the coils C_2 and C_3 remain unchanged which is shown in Fig. 5(b). On the other hand, due to rotation about the z-axis the coils C_2, C_3, C_4 and C_5 all change their orientation but coil C_1 remains unchanged as shown in Fig. 5(c).

4.3. The change in induced EMF due to translation

The change in induced emfs is calculated for the application of a gradient strength of $\frac{dG}{dt} = 4\ \mathrm{Tm^{-1}\,s^{-1}}$. The change in voltage induced within the coils due to a 10 mm shift along the x-axis is shown in Fig. 6(a). For translations along the x-axis, the change

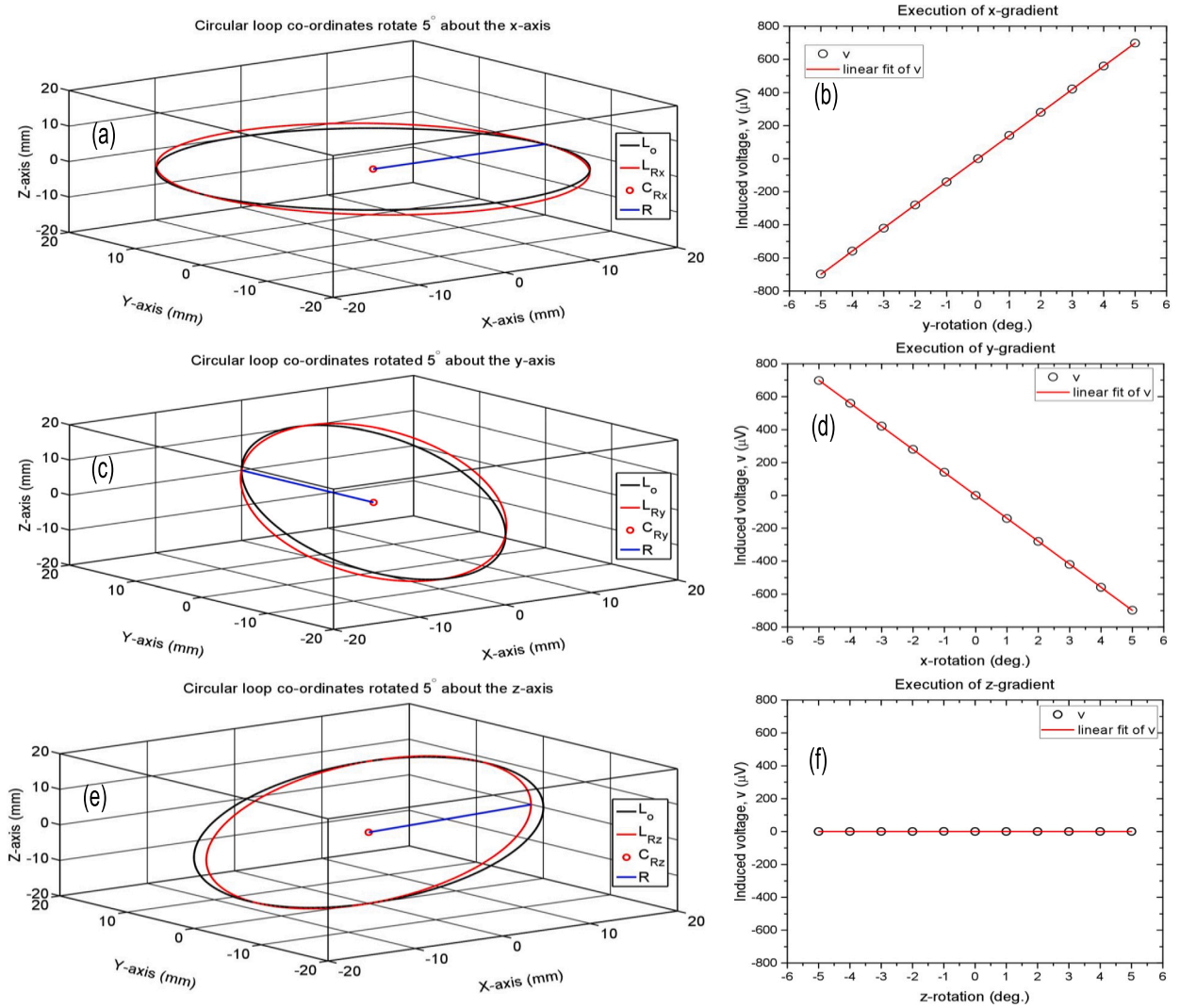

Fig. 2. Rotation about the x-, y- and z-axis. (a) A circular coil in the xy-plane and 5° rotation about the x-axis. (b) The change in induced voltage in a coil placed in the xy-plane due to rotation about the x-axis during execution of a y-gradient. (c) A circular coil in the yz-plane and its rotation (5°) about the y-axis. (d) The change in induced voltage in a coil placed in the xy-plane during execution of an x-gradient. (e) A circular coil in the zx plane and its rotation (5°) about the z-axis. (f) The change in induced voltage in a coil due to rotation about the z-axis during execution of x-, y- and z-gradients. The change in induced voltage in the coil is linear up to a rotation of 5°. However, there are no voltage changes in the coil due to translation along the z-direction during the execution of the z-gradient.

in induced voltage due to the application of an x-gradient occurs in coil C_1 only; for a y-gradient there are no changes; but for a z-gradient, changes occur in coils C_2 and C_3. The change in induced voltage in coil C_1 due to execution of an x-gradient is $\delta V_x = 502.65$ μV. The change in induced voltage in the coil C_1 due to a shift along the x-axis is given by the Eq. (9):

$$\delta V_1 = -g_x \times S_z \times \delta x. \tag{9}$$

Where $g_x = \frac{dG_x}{dt}$ and area of the circular coil having 10 turns is S_z. In simulation $g_x = 4$ T/m-s, area of the circular coil $S_z = 10 \times \pi R^2 = \pi(20)^2$ mm^2 and $\delta x = 10$ mm, that gives us $\delta V_1 = 502.65$ μV which is exactly what is obtained from simulation shown in Fig. 6(a). For the z-gradient, the change in voltage induced within the coils C_2 and C_3 is as follows (Eq. (10)):

$$\delta V_2 = \frac{1}{2} g_z \times S_x \times \delta x, \quad \delta V_3 = \frac{1}{2} g_z \times S_{-x} \times \delta x, \tag{10}$$

which gives us $\delta V_2 = \delta V_3 = 251.33$ μV. Calculation gives us the same result as shown in Fig. 6(a).

The change in induced voltage due a to 10 mm shift along the y-axis is shown in Fig. 6(b). In translation along the y-axis, the induced voltage due to the x-gradient changes in coil C_1 only, for the y-gradient there is no change, but for the z-gradient changes occur in coil C_4 and C_5. A change in induced voltage is observed in coil C_1 for execution of the x-gradient and in the coils C_4 and C_5 (Eq. (11)) for the z-gradient. There are no voltage change observed in the rest of the coils. In simulation $g_y = 4$ T/m-s,

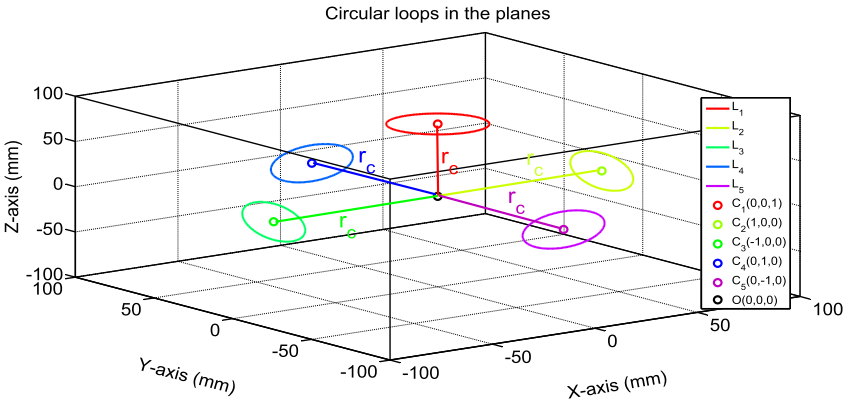

Fig. 3. A system of five loops in the planes. r_c stands for the linear distance (magnitude of the location vector) of the center of the coils from the magnetic isocenter (reference point). L_1, L_2, L_3, L_4, and L_5 indicate the circumference of the coils, and C_1, C_2, C_3, C_4, and C_5 represent the coil number as well as the coordinates of their centers.

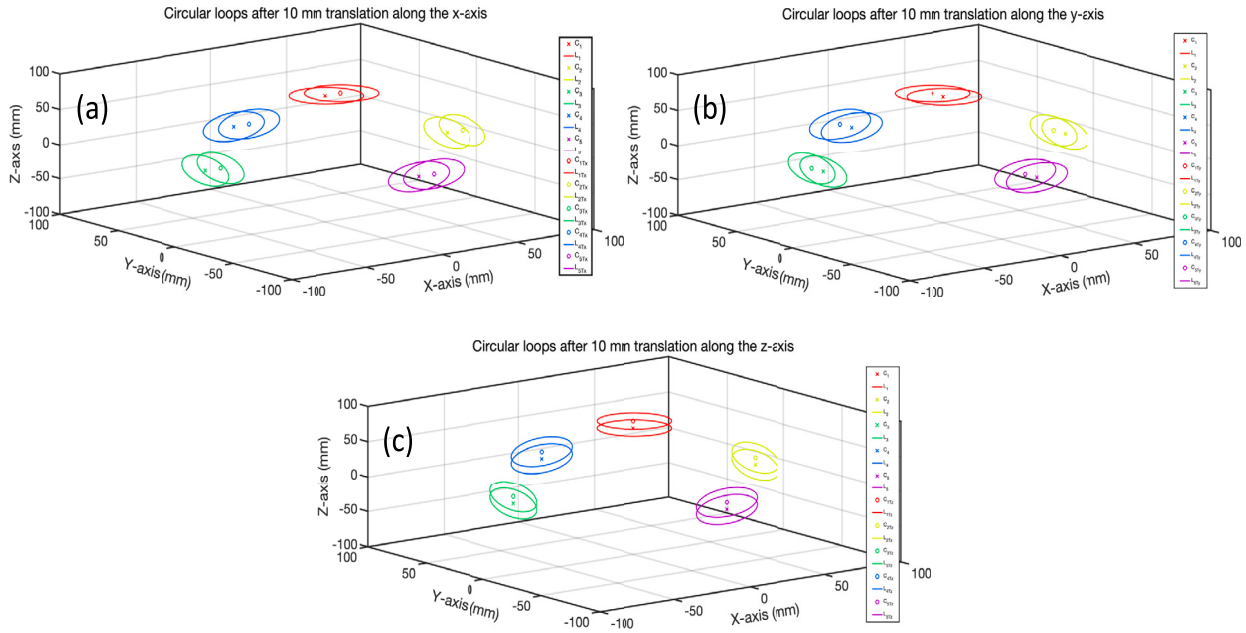

Fig. 4. Translation of the system along the three mutually perpendicular axes is shown. The centers of the coils are denoted by circle (∘) before the translation and by cross (×) after the translations. (a) Translation along the x-axis. (b) Translation along the y-axis. (c) Translation along the z-axis.

$S_z = 10 \times \pi R^2 = 10 \times \pi(20)^2$ mm^2 and $\delta y = 10$ mm, that gives us $\delta V_1 = -502.65$ μV which is exactly what is obtained from the simulation shown in Fig. 6(b).

$$\delta V_4 = -\frac{1}{2} g_z \times S_y \times \delta y, \quad \delta V_5 = -\frac{1}{2} g_z \times S_{-y} \times \delta y, \tag{11}$$

which gives us $\delta V_4 = \delta V_5 = 251.33$ μV. Calculation therefore gives us the same result as are shown in Fig. 6(b).

The change in induced voltage due to a 10 mm shift along the z-axis is shown in Fig. 6(c). In translation along the z-axis, the induced voltage due to the z-gradient changes in coil C_1 only, for the x-gradient changes occur in the coils C_2 and C_3, but for the y-gradient changes occurs in coil C_4 and coil C_5. Data shown in Fig. 6(c) also agree well with numerical calculations based on theory [49].

The change in induced voltage due to consecutive shifts along the x-axis during the application of the x- and z-gradients is shown in Fig. 7(a-c). The changes occur in coil C_1 during execution of an x-gradient and in the coils C_2 and C_3 during execution of a z-gradient, whereas no changes occur in the rest of the coils. In this case, there is no change in the induced voltage in any of the coils during execution of a y-gradient.

Induced voltage changes in the coils due to consecutive shifts along the y-axis for the application of the y- and z-gradients are shown in Fig. 7(d-f). The voltage changes occur in coil C_1 for a y-gradient and in the coils C_4 and C_5 for a z-gradient. No change is

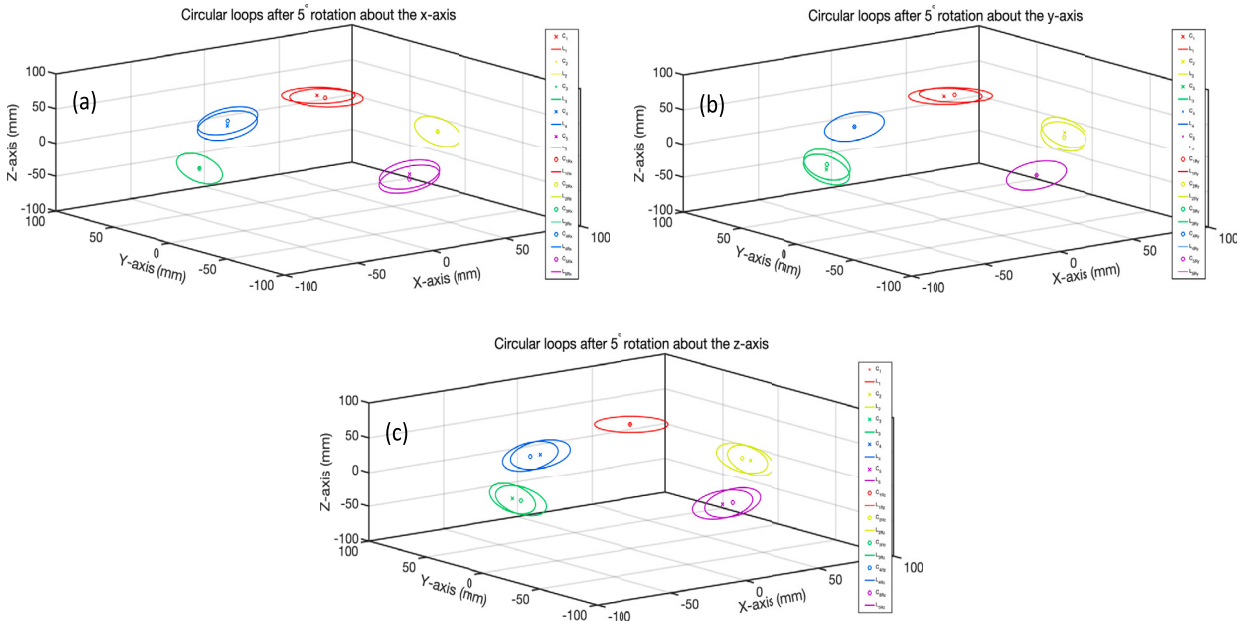

Fig. 5. Rotation of the system along the three mutually perpendicular axes is shown. The centers of the coils denoted by circle (∘) before the rotation and by cross (×) after the rotations. (a) Rotation about the x-axis. (b) Rotation about the y-axis. (c) Rotation about the z-axis. When the system is rotated about a specific axis, the centers of the coils that exist on that axis only move about the axis without changing their positions.

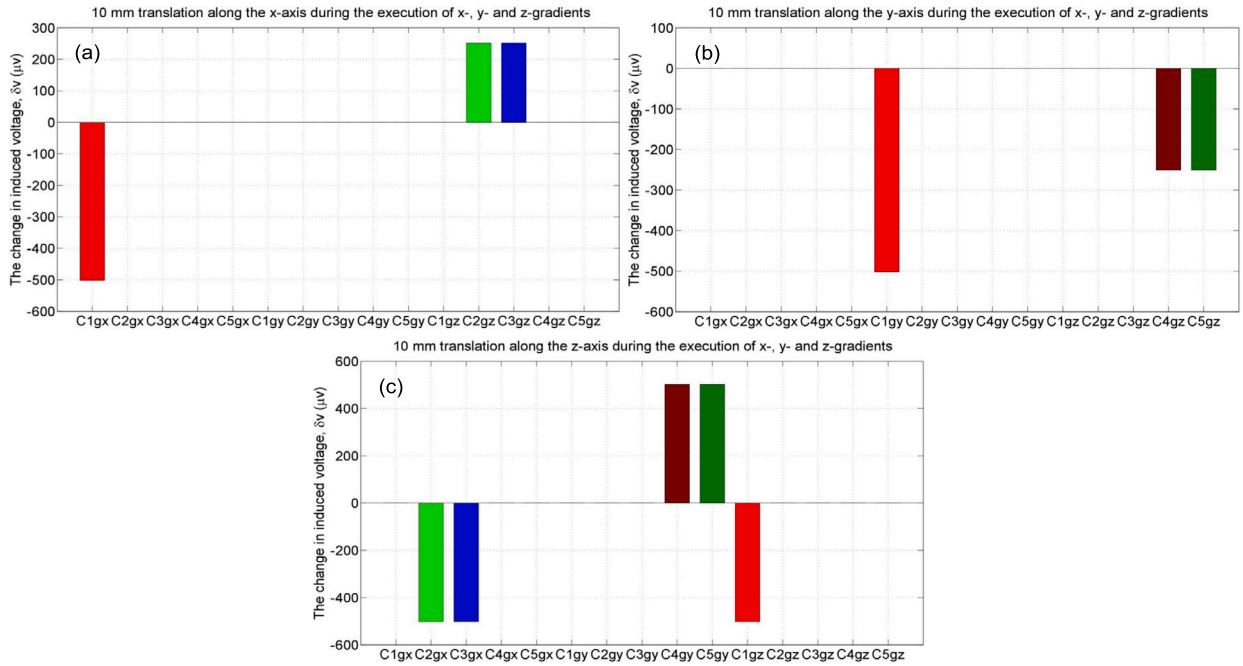

Fig. 6. The change in voltage induced (μV) in the coils by the execution of x-, y- and z-gradients. $C_n g_\alpha$ denotes the change in induced voltage in coil n (n = 1, 2, 3, 4 and 5; coil number) due to the gradient applied along the α (α = x-, y-, and z-gradient). (a) The voltage changes occurred in coil C_1 during the application of the x-gradient, and in coils C_2 and C_3 during the application of the z-gradient due to x-translation. (b) The voltage changes occurred in coil C_1 during the application of the y-gradient, and in coils C_4 and C_5 during the application of the z-gradient due to y-translation. (c) The voltage changes occurred in coil C_1 during the application of the z-gradient, and in coils C_2 and C_3 during the application of the x-gradient, and in coils C_4 and C_5 during the application of the y-gradient due to z-translation. The coils and the gradients are distinguished by color.

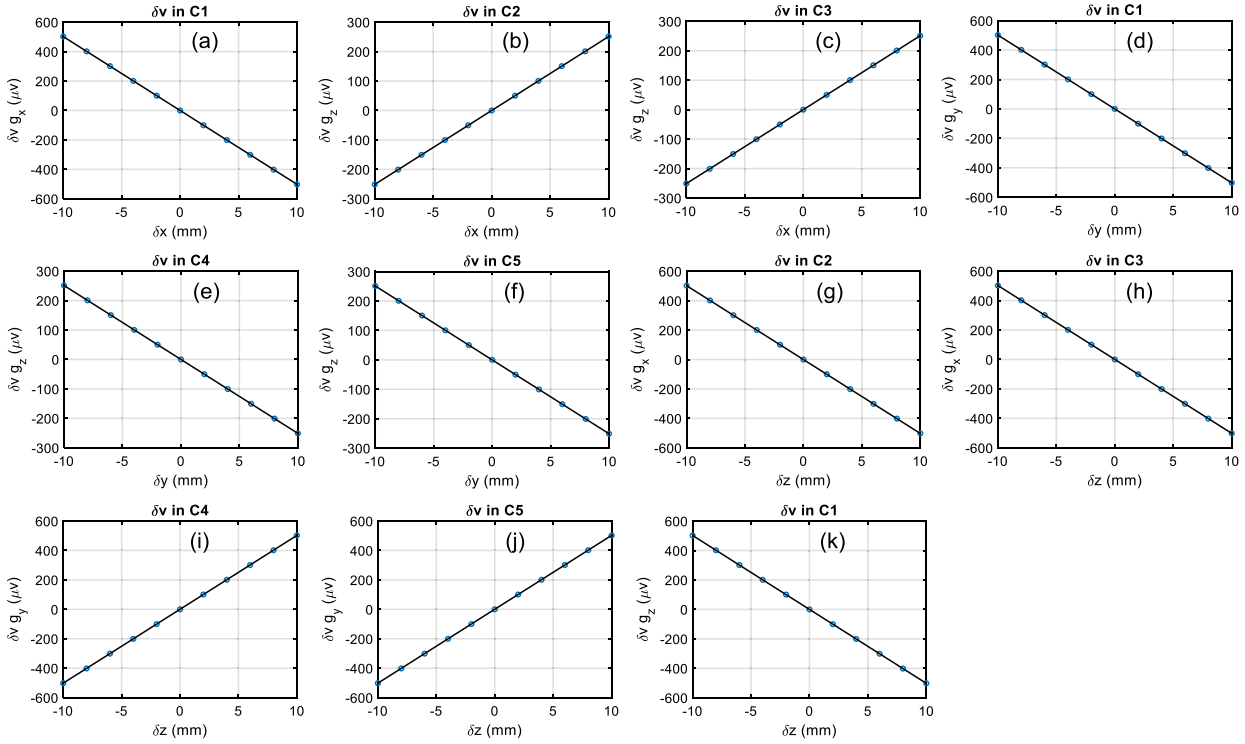

Fig. 7. The change in voltage induced (μV) in the coils due to consecutive translation along the x-, y- and z-axes by the execution of x-, y- and z-gradients. C_n and g_α denote the change in induced voltage in coil n due to the gradient applied along the α direction respectively (a) translation along the x-axis for coil C_1 exposed to an x-gradient (b) translation along the x-axis for coil C_2 exposed to an z-gradient (c) translation along the x-axis for coil C_3 exposed to an z-gradient (d) translation along the y-axis for coil C_1 exposed to an y-gradient (e) translation along the y-axis for coil C_4 exposed to an z-gradient (f) translation along the x-axis for coil C_5 exposed to an z-gradient (g) translation along the z-axis for coil C_2 exposed to an x-gradient (h) translation along the z-axis for coil C_3 exposed to an x-gradient (i) translation along the z-axis for coil C_4 exposed to an y-gradient (j) translation along the x-axis for coil C_5 exposed to an y-gradient (k) translation along the z-axis for coil C_1 exposed to an z-gradient.

observed in other coils for both of the gradients. The change in induced voltage due to a consecutive shift in the z-axis during the application of the x- and y-gradients is shown in Fig. 7(g-k). The voltage changes occur in the coils C_2 and C_3 for an x-gradient and in the coils C_4 and C_5 for a y-gradient. In this case there is no change in induced voltage in the rest of the coils for the both of the gradients. The change in induced voltage due to a consecutive shift in the z-axis because of the application of z-gradient occurs in coil C_1.

By shifting the whole system in the y-axis consecutively linear changes in induced voltages in the coils are observed. According to the theory [49], the change in induced voltage in the coil C_1 due to shift in the y-axis is given by the Eq. (12):

$$\delta V_1 = -g_y \times S_z \times \delta y. \tag{12}$$

Linear changes in induced voltage are observed due to consecutive shifts along the z-axis. One can conclude that change in induced voltage due to translation is always linear with change in position along x-, y- and z-axes. According to the theory [49], change in induced voltages in the coils due to shift in the z-axis is given by the Eqs. (13):

$$\begin{aligned} &\delta V_1 = -g_z \times S_z \times \delta z, \quad \delta V_2 = -g_x \times S_x \times \delta z \\ &\delta V_3 = -g_x \times S_{-x} \times \delta z, \quad \delta V_4 = +g_y \times S_y \times \delta z \\ &\qquad \delta V_5 = +g_y \times S_{-y} \times \delta z. \end{aligned} \tag{13}$$

In simulation $g_x = g_y = g_z = 4$ T/m-s, $S_z = S_x = S_{-x} = S_y = S_{-y} =$ Number of turns $\times \pi R^2 = 10 \times \pi(20)^2$ mm^2 and $\delta z = 10$ mm, that gives us $\delta V_1 = \delta V_2 = \delta V_3 = -502.65$ μV and $\delta V_4 = \delta V_5 = -502.65$ μV which is exactly what is obtained from the simulation shown in Fig. 7.

The change in induced voltage observed in the coils C_1, C_2 and C_3 due to the application of the x-, y- and z-gradients is shown in Fig. 7(a-c) for the case where the whole system is consecutively shifted along the x-axis. When the whole system is consecutively shifted along the y-axis the change in induced voltage occurs in the coils C_1, C_4 and C_5 due to the application of the x-, y- and z-gradients as shown in Fig. 7(d-f). The changes in induced voltage are linear and quantitatively agree with theoretical predictions. The whole system is now consecutively shifted along the z-axis and the change in induced voltage observed in the coils C_2, C_3, C_4, C_5 and C_1 due to the application of the x-, y- and z-gradients, is shown in Fig. 7(g-k).

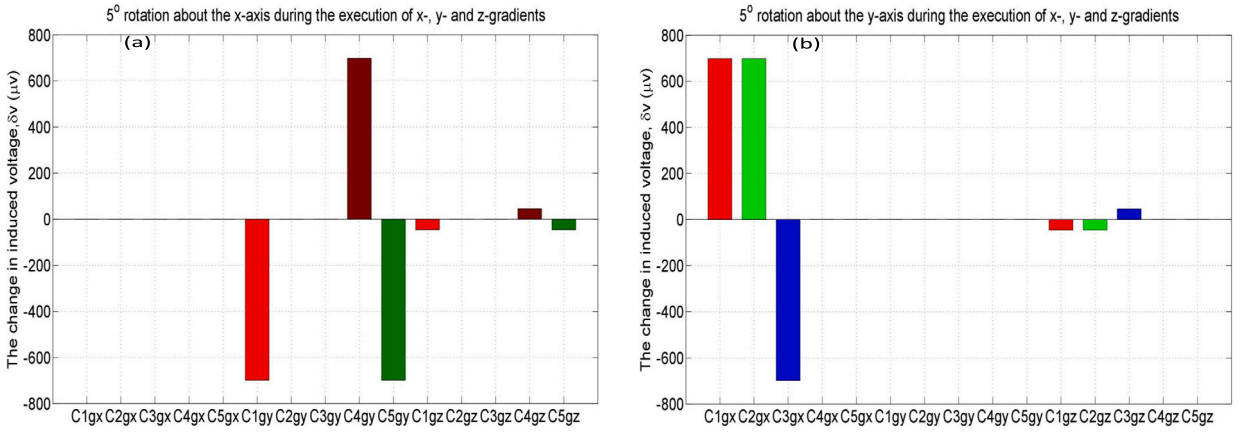

Fig. 8. The change in voltage induced (μV) in the coils by the execution of x-, y- and z-gradients. $C_n g_\alpha$ denotes the change in induced voltage in coil n (n = 1, 2, 3, 4 and 5; coil number) due to the gradient applied along the α (α = x-, y- and z-gradient). (a) The voltage changes occurred in coil C_1, C_4 and C_5 during the application of the y-gradient, and in coils C_1, C_4 and C_5 during the application of the z-gradient due to rotation about the x-axis. (b) The voltage changes occurred in coil C_1, C_2 and C_3 during the application of the x-gradient, and in coils C_1, C_2 and C_3 during the application of the z-gradient due to rotation about the y-axis. The coils and the gradients are distinguished by color.

4.4. The change in induced voltage due to rotation

The change in voltage induced within the coils due to rotations (of less than 5°) about the x- and y-axes is shown in Fig. 8. According to the theory [49], changes in the induced voltages occur in the coils C_1, C_4 and C_5 due to the application of the y-gradient because of the rotation about the x-axis is as follows (Eqs. (14)):

$$\delta V_1 = +2g_y \times z \times S_z \times \delta\phi_x, \qquad \delta V_4 = -2g_y \times y \times S_y \times \delta\phi_x,$$
$$\delta V_5 = -2g_y \times y \times S_y \times \delta\phi_x. \tag{14}$$

Where $g_y = 4$ T/m-s, $z = y = r_c = 80$ mm = coil offset, $S_y = S_{-y} = S_z$ = Number of turns (N) $\times \pi R^2 = 10 \times \pi(20)^2$ mm^2 and $\delta\phi_x = 0.0873$ radians, gives $\delta V_1 = -702.11$ μV, $\delta V_4 = 702.11$ μV and $\delta V_5 = -702.11$ μV which is exactly what is obtained from simulation as shown in Fig. 8(a).

In this case for the z-gradient changes occur in the same coils and are given by the following Eqs. (15):

$$\delta V_1 = -\frac{3}{2} g_z \times z \times S_z \times \delta\phi_x^2, \qquad \delta V_4 = \frac{3}{2} g_z \times y \times S_y \times \delta\phi_x^2,$$
$$\delta V_5 = \frac{3}{2} g_z \times y \times S_y \times \delta\phi_x^2. \tag{15}$$

Since $g_z = 4$ T/m-s, $z = y = r_c = 80$ mm = coil offset, $S_y = S_z$ = Number of turns (N) $\times \pi R^2 = 10 \times \pi(20)^2$ mm and $\delta\phi_x^2 = 7.61 \times 10^3$ radians^2, this gives us $\delta V_1 = -45.90$ μV $\delta V_4 = 45.90$ μV and $\delta V_5 = -45.90$ μV which is exactly what I get from simulation that is shown in Fig. 8(a).

On the other hand, the change in induced voltages occurs in the coils C_1, C_2 and C_3 due to rotation about the y-axis because of the application of the x-gradient as follows (Eqs. (16)):

$$\delta V_1 = -2g_x \times z \times S_z \times \delta\phi_y, \qquad \delta V_2 = 2g_x \times x \times S_x \times \delta\phi_y,$$
$$\delta V_3 = 2g_x \times x \times S_x \times \delta\phi_y, \tag{16}$$

where $g_x = 4$ T/m-s, $z = x = r_c = 80$ mm = coil offset, $S_x = S_z$ = Number of turns (N) $\times \pi R^2 = \pi(20)^2$ mm^2 and $\delta\phi_y = 0.0873$ radians, all these gives us $\delta V_1 = -702.11$ μV $\delta V_2 = -702.11$ μV and $\delta V_3 = 702.11$ μV volts which is exactly what is obtained from the simulations, as shown in Fig. 8(b).

In this case for the z-gradient changes occur in the same coils and are given by the following Eqs. (17):

$$\delta V_1 = -\frac{3}{2} g_z \times z \times S_z \times \delta\phi_y^2, \qquad \delta V_2 = \frac{3}{2} g_z \times x \times S_x \times \delta\phi_y^2,$$
$$\delta V_3 = \frac{3}{2} g_z \times x \times S_x \times \delta\phi_y^2, \tag{17}$$

where $g_z = 4$ T/m-s, $z = x = r_c = 80$ mm = coil offset, $S_x = S_z$ =Number of turns (N)$\times \pi R^2 = 10 \times \pi(20)^2$ mm^2 and $\delta\phi_y^2 = 7.61 \times 10^{-3}$ radians^{-3}, these gives us $\delta V_1 = -45.90$ μV $\delta V_2 = -45.90$ μV and $\delta V_5 = 45.90$ μV which is exactly what is obtained from simulation that is shown in Fig. 8(b). The theory and simulation [49] agree well that there is no change in the voltage induced in the coils due to rotation about the z-axis.

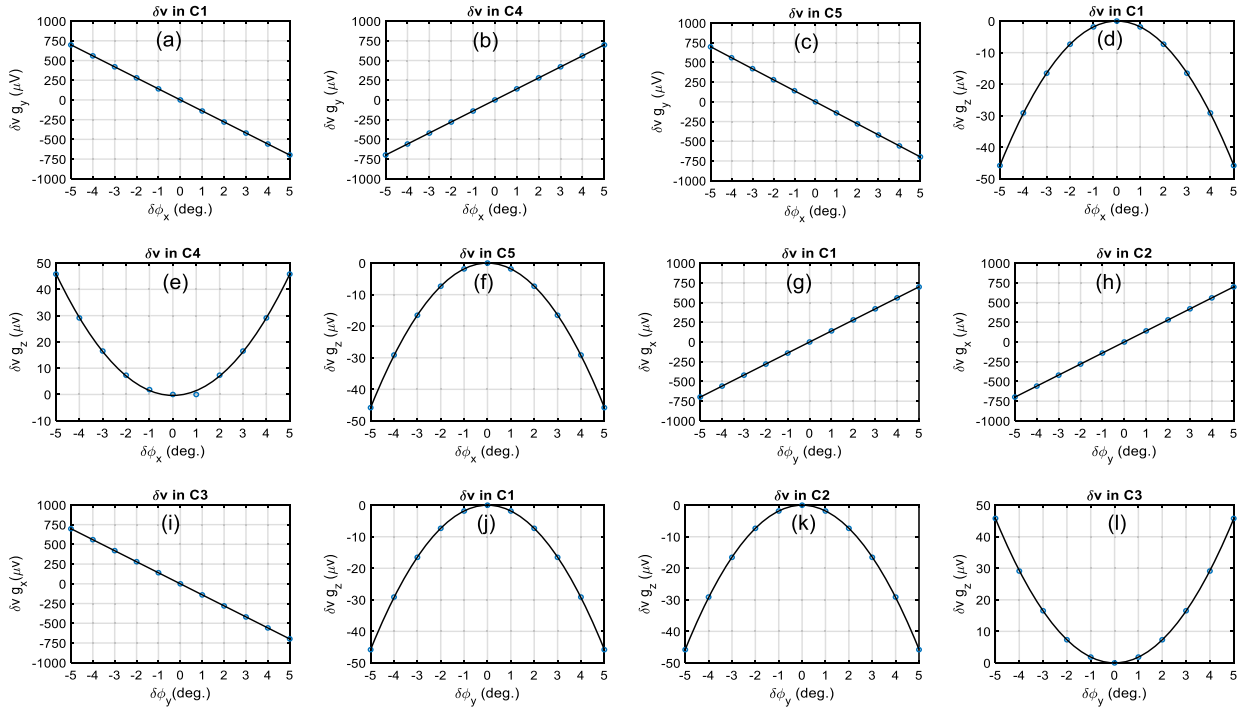

Fig. 9. The change in voltage induced (μV) in the coils due to consecutive rotation by the execution of x-, y- and z-gradients. C_n and g_α denote the change in induced voltage in coil n due to the gradient applied along the α (a) in coil C_1 due to rotation about the x-axis by the execution of y-gradient. (b) in coil C_4 due to rotation about the x-axis by the execution of y-gradient. (c) in coil C_5 due to rotation about the x-axis by the execution of y-gradient. (d) in coil C_1 due to rotation about the x-axis by the execution of z-gradient. (e) in coil C_4 due to rotation about the x-axis by the execution of z-gradient. (f) in coil C_5 due to rotation about the x-axis by the execution of z-gradient. (g) in coil C_1 due to rotation about the y-axis by the execution of x-gradient. (h) in coil C_2 due to rotation about the y-axis by the execution of x-gradient. (i) in coil C_3 due to rotation about the y-axis by the execution of z-gradient. (j) in coil C_1 due to rotation about the y-axis by the execution of z-gradient. (k) in coil C_2 due to rotation about the y-axis by the execution of z-gradient. (l) in coil C_3 due to rotation about the y-axis by the execution of z-gradient.

The changes in induced voltage in the coils due to consecutive rotation about the x-, y- and z-axes are shown in Fig. 9(a-l).

The changes in induced voltage are observed in coils C_1, C_4, and C_5 (Fig. 9(a-c)) when rotating about the x-axis during the execution of the y-gradient. Conversely, during rotation about the x-axis while executing the z-gradient, these changes occur in coils C_1, C_4, and C_5 (Fig. 9(d-f)). When examining rotation, the induced voltage changes caused by the x- and z-gradients exhibit a linear relationship with the rotation angle, whereas for the z-gradient, the change in induced voltage with respect to rotation angle follows a quadratic pattern. Similarly, changes in induced voltage are noted in coils C_1, C_2, and C_3 (Fig. 9(g-i)) during rotation about the y-axis, attributed to the execution of the x-gradient. Conversely, during rotation about the x-axis, these changes occur in coils C_1, C_2, and C_3 (Fig. 9(j-l)), and this change is due to the execution of the z-gradient. Again, when considering rotation, the induced voltage changes due to the x- and z-gradients show a linear correlation with the rotation angle, while for the z-gradient, the change in induced voltage with respect to rotation angle follows a quadratic pattern.

While the voltage alteration induced within the coils due to rotation around the x and y-axes as a result of applying the z-gradient follows a quadratic pattern with respect to the rotation angle, the changes are small for small rotation angles ($\phi \leq 5°$). Analyzing the induced voltage data obtained from simulation and by using basic linear fittings one can obtain the corresponding equations. A system of linear equations is developed by basic linear fittings. The change in positions and orientations of the coils can then be found by solving this system of linear equations.

4.5. Estimated movement parameters

The fluctuations in induced voltages within the set of 5-coils while executing the 3-gradients, resulting from both rotations and translations, are computed. Through the utilization of a system of linear equations and a calibration matrix, we derive estimations for the five motion parameters. Comparison between the actual movements and the movements calculated from simulation by inverting the matrix equation is shown in Fig. 10. Fig. 10(a) shows the 7 sets of estimated parameters where there are no zero terms in the actual movements in any direction. On the other hand, in Fig. 10(b) a few zero terms in the actual movements in translation or rotation are included. In both cases, actual and estimated movement parameters have a reasonably good agreement.

Without adding any noise voltage to the changes in induced voltage, the estimated movements parameters have maximum errors in translations (~ 0.3 mm) and in rotations ($\sim 0.05°$), as shown in Fig. 11(a). In this case the actual translation is 10 mm and rotation is 5°.

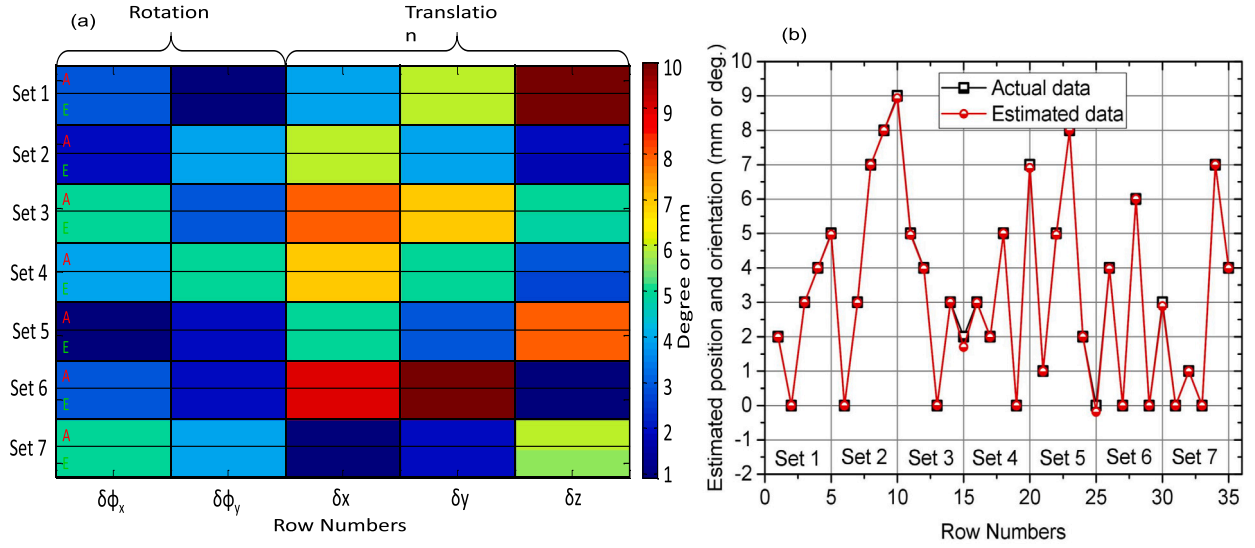

Fig. 10. The real motion parameters compared to the parameters obtained through numerical simulation by assessing alterations in the voltage induced within the coils as a result of the coils' translation and rotation while the x-, y-, and z-gradients are applied. (a) Data shows the actual and estimated movement parameters where there is no zero terms in the actual movements. Rows A and E represent actual and estimated movements, respectively. Columns 1 and 2 are for rotation about the x- and y-axes, respectively, while columns 3, 4, and 5 represent translation along the x-, y-, and z-axes. There are five sets of movement parameters, each consisting of five parameters (two for rotation and three for translation). (b) Data represents actual (black) and estimated (red) movement parameters where there is a few zero terms in the actual movements. There are five sets of movement parameters, each consisting of five parameters (two for rotation and three for translation). The unit of the error bar is degrees (for rotation) or mm (for translation).

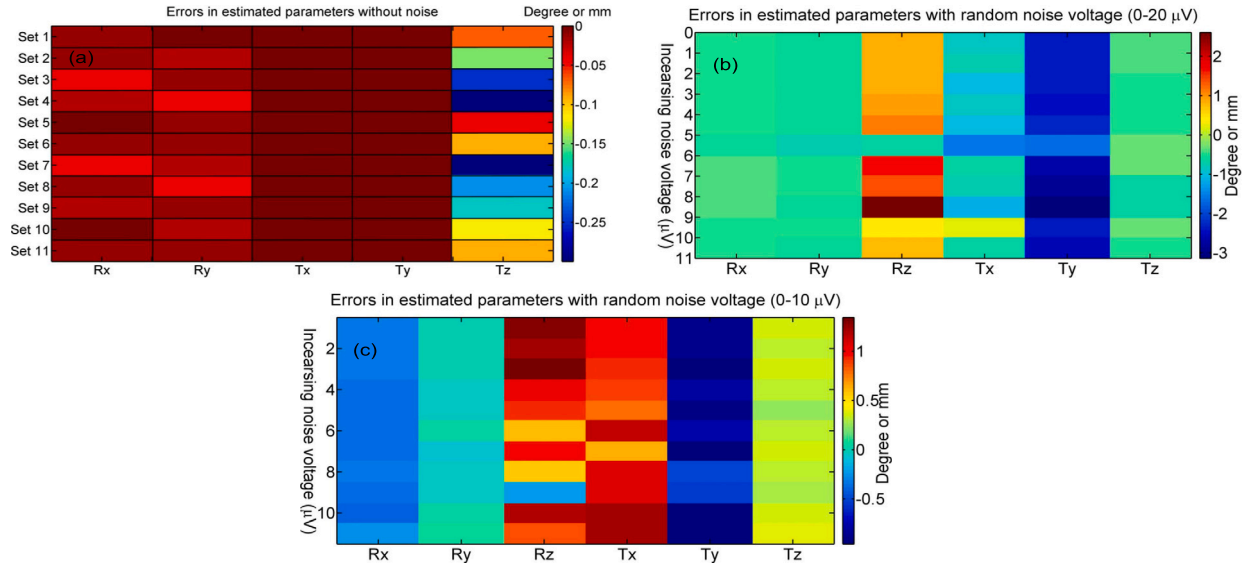

Fig. 11. In the illustration, Rx and Ry stand for rotation, while Tx, Ty, and Tz stand for translation. (a) Errors in the calculated motion parameters derived from induced voltages in the coils caused by translation and rotation in the absence of added noise voltages. Estimated inaccuracies in the Position and Orientation in Space Estimation (POSE) resulting from calculated induced voltages due to translation and rotation with incremental noise levels ranging from (0-20 μV) in (b). (b) and reducing noise level (0-10 μV) in (c). The unit of error bar is degree (rotation) or mm (translation).

A random noise voltage ranging from 0-20 μV is introduced into the computed voltage, as a result errors are observed in the estimated parameters that are shown in Fig. 11(b). A reduced random voltage, 0-10 μV is added and the errors in estimated parameters are calculated and represented in Fig. 11(c). In spite of the addition of a random noise voltage (0-10 μV), the voltage data gives us a good estimation of the change in POSE of the coils. Even after, addition of noise voltage (0-20 μV) estimated parameters do not blow up.

For planar coils, there is no voltage induced in the coils 4 and 5 during execution of an x-gradient and in the coils 1 and 3 during execution of an y-gradient due to translation along the x-, y- and z-axes and rotation about the x-, y- and z-axes. Moreover, no voltage is induced in any coils due to z-rotation.

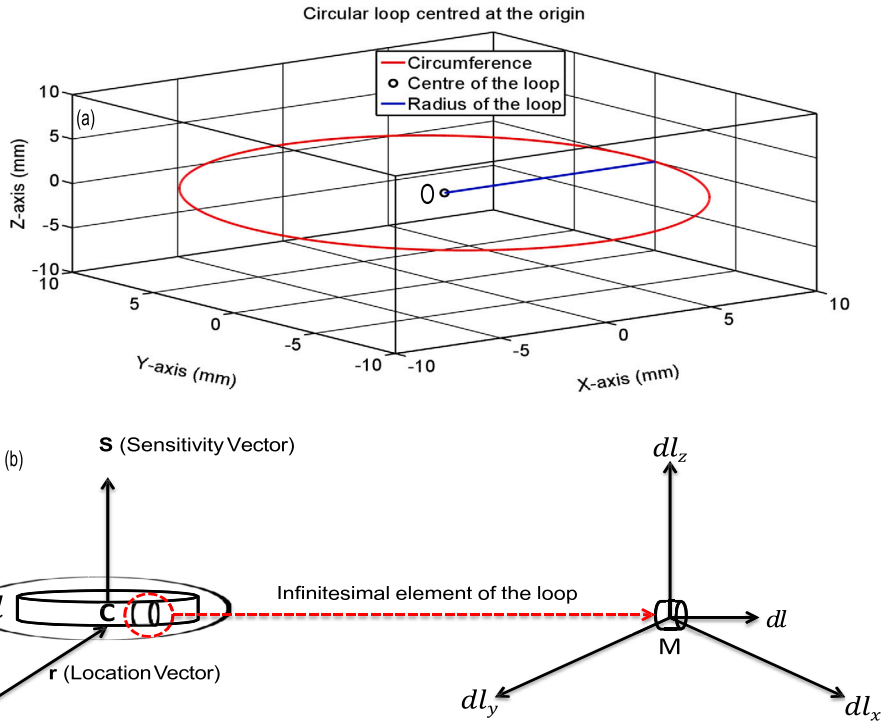

Fig. 12. (a) A circular loop centered at the origin in the xy-plane. (b) A closed circular loop with a location vector **r** and a sensitivity vector **S**, with a perimeter of length l and an infinitesimal element of length dl (zoomed-in portion). dl (dl_x, dl_y and dl_z) resolved in three mutually perpendicular directions.

To evaluate the feasibility of the simulation, a pilot experiment was conducted. The system performed well, as demonstrated by an example of the gradient pre-pulse obtained from coil C1 during the execution of x-gradients, shown in Fig. 13. To assess the presence of any distortion or artifacts in the signal picked up by the coils, we also tested the system using the EPI sequence. Fig. 14 shows a representative EPI signal obtained from coil C1.

5. Discussion

Electromagnetic tracking, often referred to as EMF-based motion tracking, is a method that employs electromagnetic fields for monitoring the movement of a solid object, such as the human head, within an MR scanner. This technique has several advantages over other motion tracking methods, such as optical tracking or accelerometer-based tracking, including the ability to track motion in real-time, without the need for line-of-sight, and without interfering with the MR image acquisition process.

Several studies have investigated the use of EMF-based motion tracking in MRI, and have shown promising results. For example, a study by Kober et al. [24] compared the accuracy of EMF-based tracking with optical tracking in a group of healthy volunteers performing head movements inside an MR scanner. They found that the EMF-based tracking was highly accurate, with a mean error of less than 0.5 mm for translation and less than 0.5 degrees for rotation.

Another study by Zaitsev et al. [16] evaluated the feasibility of using EMF-based tracking for real-time motion correction in functional MRI (fMRI). They found that the EMF-based tracking was able to detect head motion with high accuracy and could be used to implement real-time motion correction during fMRI scans, which led to improved image quality and reduced artifacts.

Despite these promising results, there are some limitations to EMF-based tracking, including sensitivity to metallic objects, potential for interference with other devices, and the need for careful calibration to ensure accuracy. However, ongoing research is aimed at addressing these limitations and improving the performance of EMF-based motion tracking in MRI.

In this preliminary study, circular coils were generated in a specific plane as shown in Fig. 12(a). Additionally, circular loops were generated in the xy, yz, and zx planes. The change in voltage induced within the coils was calculated due to translation and rotation caused by the application of x-, y-, and z-gradients.

A system of five coils was generated in the planes of a cubic box, as shown in Fig. 3. Coils C_1, C_2, and C_3 are sensitive to x-translation, while coils C_1, C_4, and C_5 are sensitive to y-translation, and all five coils are sensitive to z-translation during the execution of x-, y-, and z-gradients. Additionally, coils C_1, C_4, and C_5 are sensitive to x-rotations during the execution of y- and z-gradients, while coils C_1, C_2, and C_3 are sensitive to y-rotation during the execution of x- and z-gradients. None of the coils is sensitive to z-rotations during the execution of any gradient. The sensitivity of the coils to translation along the three axes and rotation about the three axes during the execution of x-, y-, and z-gradients is summarized in Table 2.

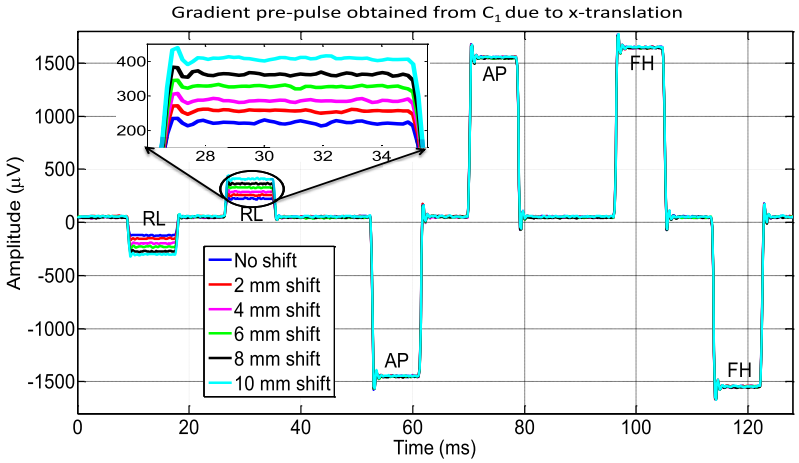

Fig. 13. Data represents the change in induced voltage during execution of gradient pre-pulses along/about RL, AP and FH axes. The change in induced voltage recorded on coil C_1 due to translation along the RL.

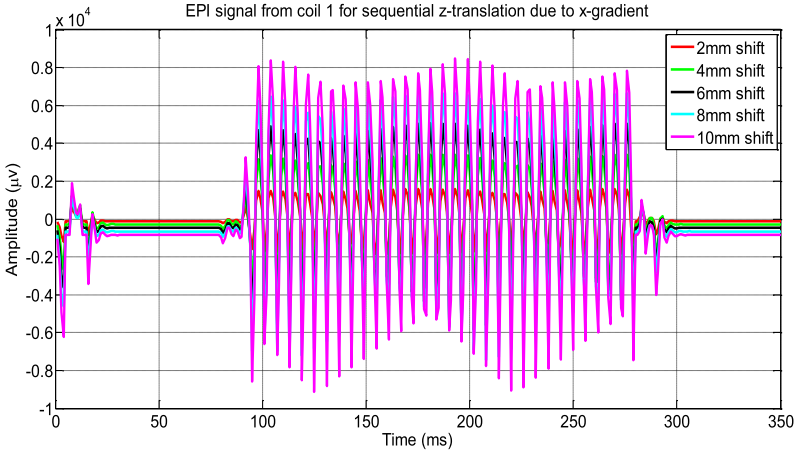

Fig. 14. The EPI signal from coil C_1 was acquired during the execution of an RL-gradient pre-pulse, which induced translation along the x-axis.

Table 2
Sensitivity of the planar coils with respect to the movements and the applied gradients.

	x-translation	y-translation	z-translation	x-rotation	y-rotation	z-rotation
x-gradient	C_1	0	C_2, C_3	C_1, C_4, C_5	0	0
y-gradient		C_1	C_4, C_5	0	C_1, C_2, C_3	0
z-gradient	C_2, C_3	C_4, C_5	C_1	C_1, C_4, C_5	C_1, C_2, C_3	0

Linear fitting was performed to relate The change in voltage induced within the coils with the change in POSE of the coils, yielding a system of linear equations (Ax = V) with a calibration matrix A. The slopes of the graphs were used to form the calibration/coefficient matrix, which was then pseudo-inverted ('pinv') to estimate the changes in movement parameters. While z-rotations cannot be estimated accurately using this method, the other five movement parameters can be estimated with reasonable accuracy. Although noise voltages can affect the estimated parameters, experiments have shown that random noise voltage ranging from 0 to 20 μV produces acceptable errors in the measured voltages.

Voltage fluctuations within the coils are computed to gauge alterations in position (POSE). To gauge how noise voltage affects the estimated motion parameters, we introduce random noise voltage into the calculated voltage, then re-estimate the parameters. It's worth noting that when the z-gradient is applied, the change in coil-induced voltage due to rotation around the x and y axes is quadratic but relatively insignificant compared to other translation and rotation alterations. In this scenario, the voltage change resulting from x and y-axis rotation is much smaller than the voltage change due to translation. Furthermore, the change in induced voltage closely approximates the noise voltage, making the linear voltage change more prominent than the quadratic change.

Even when there's substantial translation (a few centimeters), the fluctuations in coil-induced voltage exhibit a linear relationship. Likewise, when rotating around the x and y axes, the changes in coil-induced voltage while applying x and y gradients follow a linear pattern in relation to the rotation angle. However, when executing the z-gradient, the changes in coil-induced voltage

become quadratic. This linear behavior of voltage changes caused by translation and rotation enables accurate calibration of these movements. In cases of significant rotation (>5°), the linearity diminishes, but it's still possible to reasonably estimate motion parameters for rotations up to 10° using any of the methods available. Within the bounds of linearity, precise estimation of changes in POSE (Position and Orientation in Space) of the coils is feasible. Nevertheless, there are certain constraints, such as dealing with substantial rotations and the attachment of coils to the head. It is assumed that extensive rotations within head coils are unlikely, which may limit the applicability of these results in extreme scenarios. Ongoing experimental research is being conducted on this methodology [49,50].

While there is no universally accepted gold standard method for motion tracking techniques, several established methods have been developed that offer partial solutions to the problem. Among these methods, optical motion capture systems are considered to be one of the best. Although they can provide accurate estimates up to 1 mm, they require the line of sight of the marker, which may limit their application in some settings.

This simulation relies on intrinsic gradients and necessitates only MR-compatible EEG equipment as supplementary hardware. It operates without the need for a direct line of sight or sequence adjustments and can provide POSE estimations of comparable precision to well-established methods.

To verify the precision and dependability of our simulation approach of EMF-based motion tracking, we used predetermined data consisting of specific movements along the six degrees of freedom, including translation along x, y, z and rotation about x, y, z. We evaluated the accuracy of our approach by testing whether a generalized linear model (Ax = V) could accurately estimate the POSE of the head for a variety of data sets. Since this is a preliminary study, we have assessed the accuracy of our approach using the root-mean-square error (RMSE) metric. The uncertainty associated with our estimates has also been quantified using the RMSE metric [30].

Another limitation is the effect of noise voltage on the accuracy of the induced voltage measurements in the coils. To test this, we added random noise voltage to the induced voltage signals and found that even with the addition of 20 μV of noise, the model was still able to accurately estimate the movement parameters.

We utilized predetermined datasets consisting of specific movements along the six degrees of freedom and estimated the movements using the calibration matrix A from the Ax = V system of linear equations to verify the precision and dependability of our simulation approach. In addition, we conducted experiments (unpublished) to assess the impact of noise voltage on the accuracy of the induced voltage measurements in the coils. Although these methods indirectly demonstrate the stability and consistency of our simulation approach for head motion tracking inside an MR scanner, further testing and evaluation may be necessary to fully assess its robustness and sensitivity. However, coil sensitivity was studied in theory [30].

The results obtained from the pilot experiment are promising, as no artifacts, distortion, or phase shift were observed in either the gradient pre-pulse or EPI sequence.

Overall, Our method (EMF-based motion tracking without sequence modification) is a promising technique for improving the accuracy and reproducibility of MRI scans, particularly in studies involving motion-sensitive imaging techniques such as fMRI.

6. Methods

In this study, the simulation was conducted using a 3T MR scanner, which is a commonly used field strength for clinical imaging. The native gradients of the MR scanner were considered in the simulation, which are responsible for producing the magnetic field gradients necessary for spatial encoding of the MR signal. Additionally, gradient pre-pulses were also taken into account in the simulation. The POSE of the subject within the MR scanner and the comfort of the patient were taken into consideration during the simulation.

A circular coil in the specific plane is generated to calculate the variation in induced EMF in the coils during translations along the x-, y- and z-axes during time varying x-, y- and z-gradients. A system of five coils confined to four of the surfaces of a cube is generated and the same calculations are done for the five coils. A linear model is used to estimate the change in POSE of the coils from the calculated induced voltage changes.

The graphs and figures were generated using MATLAB version 9.2 (R2017a) by The MathWorks Inc., located in Natick, Massachusetts. The errors in the estimated parameters were calculated using predetermined parameters as well as the root-mean-square error (RMSE).

6.1. Simulation parameters

A few parameters are used for simulations of the voltage induced in a loop. These are: the number of turns in each loop n; the radius of the loop R, the amplitudes of the x-, y- and z-gradients G_x, G_y and G_z, the frequency (ω) at which the gradient changes in time, the number of points around the loop N. The translations along the x-, y- and z-axes are δx, δy and δz respectively, the rotations about the x-, y- and z-axes are $\delta\phi_x$, $\delta\phi_y$ and $\delta\phi_z$ respectively. In this study the number of turns are taken n = 10, radius R = 20 mm; the gradient amplitudes $G_x = G_y = G_z = G = 0.636 \times 10^{-3}$ T/m, frequency $\omega = (2\pi \times 1000)$ Hz, ($\frac{dG}{dt} = 4$ T/m-s), number points around the loop N = 200, maximum translation along the x-, y- and z-axes $\delta x = \delta y = \delta z = 10$ mm and maximum rotation about the x-, y- and z-axes $\delta\phi_x = \delta\phi_y = \delta\phi_z = 5°$.

6.2. EMF in a circular coil

A circular loop is formed from a small set of line elements in a given radius, as shown in Fig. 12 (a), where O is the center of the loop. One can obtain the alteration in induced EMF in the loop during translation, rotation and change in size of the loop in a time-varying magnetic-field gradient.

To describe rigid body movement completely one has to handle six movement parameters, three are for translation and three are for rotational motion.

The voltage is calculated by numerical integration of the vector potential, **A**, over a closed circular loop shown in Eq. (1). Let us consider a closed circular loop of circumference l and an infinitesimal length of the circumference is dl, where $dl = \hat{i}dl_x + \hat{j}dl_y + \hat{k}dl_z$, as shown in Fig. 12(b).

In Fig. 12(b), C is the center of the loop, **r** is the location vector, **S** is the sensitivity vector, i.e. a vector normal to the surface of the loop and M is the mid-point of the infinitesimal length of the loop. For simulation, N points are taken round the circumference that gives us N infinitesimal elements. The vector potential is determined or computed at the halfway point of every element. By summing up the contributions from all the elements the total induced voltage in the loop is calculated due to the execution of the time-varying magnetic field gradients along the x-, y- and z-directions. The general equation for change in induced voltage in a coil due to the applications of the magnetic field gradients is given as follows (Eq. (18)):

$$V = \sum V_{g_x} + V_{g_y} + V_{g_z}, \tag{18}$$

where subscripts g_x, g_y and g_z indicate the x, y and z-gradients respectively.

6.3. Movement parameters

A calibration matrix is formed by using the slopes obtained from the linear fittings of the system of linear equations. To estimate the movement parameters, both cued and random movements of the coils are performed, and the changes in the induced voltage in the coils are calculated. The pseudoinverse (using the 'pinv' function built-in to MATLAB 2017a) is used to estimate the movement parameters from the calculated changes in induced voltage. To evaluate the robustness of the method, random noise voltages of magnitudes 0-10 μV and 0-20 μV are added, and the estimated movement parameters are compared to the known values."

6.4. Viability of simulation and modeling

We conducted evaluations on our system to ascertain its capability to measure induced voltage in the coils without disruptions caused by artifacts, distortions, or changes in phase. To assess this, we performed a preliminary experiment where we measured alterations in induced voltage in a coil resulting from translation or rotation along the x-, y-, and z-axes while executing three gradient pre-pulses. Additionally, we assessed our system's performance using the EPI sequence.

7. Conclusion

A new method has been developed in this initial study to track the movement of a rigid object (the head) within an MRI scanner by detecting alterations in EMF induced in coils mounted on the head, when they are in a specific spatial plane. This approach is quick and compatible with the MR system, relying on the coils' geometry and the magnetic field gradients that vary over time. The software is relatively easy to use and can accurately measure position with an error of approximately ≈ 0.3 mm and orientation with an error of around $\approx 0.05°$. While it was designed with EPI pulse sequence and fMRI in mind, in principle it can be adapted to any MRI application where rigid body motion is visible. There is no need to modify clinical MR sequences to use this EMF-based tracking system. By transmitting six rigid-body motion parameters to the pulse programmer, prospective motion correction could be implemented by monitoring head movement inside the MR scanner.

Overall, EMF base head movement tracking inside MR scanner shows promise as a technology that can greatly improve the accuracy and reproducibility of MRI scans. However, the system's accuracy and reliability depend on various factors such as coil design, calibration procedures, and experimental controls to ensure the results' validity. Further research is necessary to optimize the EMF base head movement tracking technology and assess its effectiveness in different clinical settings. Nonetheless, the potential benefits of this technology make it an encouraging research area for enhancing MRI scan quality and efficiency.

Abbreviation

- DWI: diffusion-weighted imaging
- EEG: electroencephalography
- EM: electromagnetic
- EMF: electromagnetic field
- EPI: echo planar imaging
- fMRI: functional magnetic resonance imaging
- MR: magnetic resonance

- MRI: magnetic resonance imaging
- MPRAGE: magnetization prepared rapid gradient echo
- NMR: nuclear magnetic resonance
- POSE: position and orientation
- RL: right-left

CRediT authorship contribution statement

E. H. Bhuiyan and P. M. Glover conceived and designed the experiments; E. H. Bhuiyan and M. E. H. Chowdhury, performed the experiments; E. H. Bhuiyan and M. E. H. Chowdhury analyzed and interpreted the data; E. H. Bhuiyan, E. H. Chowdhury and P. M. Glover contributed materials, analysis tools and data; E. H. Bhuiyan wrote the paper. Each of the authors has made substantial contributions to both the advancement and the composition of this article.

Declaration of competing interest

The authors have no conflict of interest.

Data availability

Data will be made available on request.

Acknowledgements

E. H. Bhuiyan acknowledges with gratitude Professor Richard W. Bowtell of the Sir Peter Mansfield Imaging Centre, School of Physics and Astronomy, University of Nottingham, for his valuable discussion during this study.

References

[1] F. Godenschweger, U. Kägebein, D. Stucht, et al., Motion correction in MRI of the brain, Phys. Med. Biol. 61 (2016) R32–R56.
[2] P.L. Young, L.A. Olsen, The Healthcare Imperative: Lowering Costs and Improving Outcomes: Workshop Series Summary, Roundtable on Evidence-Based Medicine, ISBN 0-309-14434-5, 2010, 668 pages, 6 × 9.
[3] R.A. Poldrack, E.J. Paré-Blagoev, P.E. Grant, Pediatric functional magnetic resonance imaging: progress and challenges, Top. Magn. Reson. Imaging 13 (2002) 61–70.
[4] T.T. Brown, J.M. Kuperman, M. Erhart, et al., Prospective motion correction of high-resolution magnetic resonance imaging data in children, NeuroImage 53 (2010) 139–145.
[5] E. Seto, G. Sela, W.E. Mcllroy, S.E. Black, W.R. Staines, M.J. Bronskill, A.R. McIntosh, S.J. Graham, Quantifying head motion associated with motor tasks used in fMRI, NeuroImage 14 (2001) 284–297.
[6] C.J.C. Cochrane, K.P.K. Ebmeier, Diffusion tensor imaging in parkinsonian syndromes: a systematic review and meta-analysis, Neurology 80 (9) (2013) 857–864.
[7] G.T. Stebbins, C.M. Murphy, Diffusion tensor imaging in Alzheimer's disease and mild cognitive impairment, Behav. Neurol. 21 (1) (2009) 39–49.
[8] I. Bohanna, N. Georgiou-Karistianis, A. Hannan, G. Egan, Magnetic resonance imaging as an approach towards identifying neuropathological biomarkers for Huntington's disease, Brains Res. Rev. 58 (1) (2008) 209.
[9] M. Inglese, M. Bester, Diffusion imaging in multiple sclerosis: research and clinical implications, NMR Biomed. 23 (7) (2010) 865–872.
[10] J. Maclaren, M. Herbst, O. Speck, M. Zaitsev, Prospective motion correction in brain imaging: a review, Magn. Reson. Med. 69 (2013) 621–636.
[11] A. Roth, E. Nevo, et al., Method and apparatus to estimate location and orientation of objects during magnetic resonance imaging, US Patent 9,037,213 B2.
[12] C.L. Dumoulin, R.D. Darrow, J.F. Schenck, S.P. Souza, Tracking system to follow the position and orientation of a device with radiofrequency field gradients, US Patent 5,211,165.
[13] T.E. Wallace, S.K. Warfield, O. Afacan, Robust retrospective correction of 3D golden-ratio radial MRI using electromagnetic tracking, Proc. Int. Soc. Magn. Reson. Med. 27 (2019) 4429.
[14] M.G. Spangler-Bickell, M.M. Khalighi, C. Hoo, et al., Rigid motion correction for brain PET/MR imaging using optical tracking, IEEE Trans. Radiat. Plasma Med. Sci. 3 (4) (2019) 498–503.
[15] J.G. Pipe, Motion correction with PROPELLER MRI: application to head motion and free-breathing cardiac imaging, Magn. Reson. Med. 42 (1999) 963–969.
[16] M. Zaitsev, C. Dold, G. Sakas, J. Hennig, O. Speck, Magnetic resonance imaging of freely moving objects: prospective real-time motion correction using an external optical motion tracking system, NeuroImage 31 (2006) 1038–1050.
[17] N. White, C. Roddey, A. Shankaranarayanan, et al., PROMO: real-time prospective motion correction in MRI using image-based tracking, Magn. Reson. Med. 63 (2010) 91–105.
[18] T.S. Sachs, C.H. Meyer, B.S. Hu, J. Kohli, D.G. Nishimura, A. Macovski, Real-time motion detection in spiral MRI using navigators, Magn. Reson. Med. 32 (1994) 639–645.
[19] L. Qin, Ehud J. Schmidt, Z.T.H. Tse, J. Santos, W.S. Hoge, C. Tempany-Afdhal, K. Butts-Pauly, C.L. Dumoulin, Prospective motion correction using tracking coils, Magn. Reson. Med. 69 (3) (2013) 749–759.
[20] M. Andersen, K.H. Madsen, L.G. Hanson, Prospective motion correction for MRI using EEG-equipment, Proc. Int. Soc. Magn. Reson. Med. 24 (2016) 4254.
[21] L. Qin, P. van Gelderen, J.A. Derbyshire, et al., Prospective head movement correction for high resolution MRI using an in-bore optical tracking system, Magn. Reson. Med. 62 (4) (2009) 924–934.
[22] C. Wildey, D.L. MacFarlane, A. Goyal, K. Gopinath, S. Cheshkov, R. Briggs, Single-camera motion measurement and monitoring for magnetic resonance applications, Appl. Opt. 50 (14) (2011) 2088–2097.
[23] J. Maclaren, M. Aksoy, R. Bammer, Contact-Free Physiological Monitoring During Simultaneous Magnetic Resonance Imaging, US patent 0331239 A1, 2016.
[24] T. Kober, P.J.P. Marques, R. Gruetter, G. Krueger, Head motion detection using FID navigators, Magn. Reson. Med. 66 (2011) 135–143.
[25] Dr. Rasmus Birn, Device for tracking Head Motion in an MRI Simulator, PhD Thesis, University of Wisconsin-Madison Department of Biomedical Engineering, 2012.

[26] M.B. Ooi, S. Krueger, W.J. Thomas, T.R. Brown, Real-time intra-volume motion correction in EPI using active markers, Proc. Int. Soc. Magn. Reson. Med. 18 (2010).
[27] J. Maclaren, R. Boegle, M. Herbst, J. Hennig, M. Zaitsev, Head pose prediction for prospectively-corrected EPI during rapid subject motion, Proc. Int. Soc. Magn. Reson. Med. 18 (2010).
[28] O. Speck, J. Hennig, M. Zaitsev, Prospective real-time slice-by-slice motion correction for fMRI in freely moving subjects, Magn. Reson. Mater. Phys. Biol. Med. 19 (2006) 55–61.
[29] R. Boegle, J. Maclaren, M. Zaitsev, Combining prospective motion correction and distortion correction for EPI: towards a comprehensive correction of motion and susceptibility-induced artifacts, Magn. Reson. Mater. Phys. Biol. Med. 23 (2010) 263–273.
[30] E.H. Bhuiyan, M.E.H. Chowdhury, P.M. Glover, Feasibility of tracking involuntary head movement for MRI using a coil as a magnetic dipole in a time-varying gradient, Magn. Reson. Imaging 101 (63) (2023) 76–89.
[31] S. Thesen, O. Heid, E. Mueller, L.R. Schad, Prospective acquisition correction for head motion with image-based tracking for real-time fMRI, Magn. Reson. Med. 44 (3) (2000) 457–465.
[32] C. Liu, R. Bammer, D.H. Kim, M.E. Moseley, T.R. Brown, Real-time MR imaging with a fully signal-integrated steerable optical camera for motion correction, Magn. Reson. Med. 61 (4) (2009) 981–988.
[33] A.K. Heye, H.P. Fautz, D. Vidaurre, Deep learning-based motion correction for functional MRI using a single-camera optical tracking system, Magn. Reson. Med. 87 (2) (2022) 844–856.
[34] M. Laustsen, M. Andersen, R. Xue, K.H. Madsen, L.G. Hanson, Tracking of rigid head motion during MRI using an EEG system, Magn. Reson. Med. 88 (2) (2022) 986–1001.
[35] A. Roth, E. Nevo, Method and apparatus to estimate location and orientation of objects during magnetic resonance imaging, US Patent 9,037,213, 2015.
[36] R. Frost, P. Wighton, F.I. Karahanoğlu, et al., Markerless high-frequency prospective motion correction for neuroanatomical MRI, Magn. Reson. Med. 82 (2019) 126–144.
[37] J. Yu, C. Li, K. Lou, C. Wei, Q. Liu, Embedding decomposition for artifacts removal in EEG signals, J. Neural Eng. 19 (2022) 026052.
[38] Z. Chen, H. Wang, Z. Lu, Real-time motion correction of EEG signals using convolutional neural networks, IEEE Trans. Neural Syst. Rehabil. Eng. 30 (2022) 550–560.
[39] O. Afacan, T.E. Wallace, S.K. Warfield, Retrospective correction of head motion using measurements from an electromagnetic tracker, Magn. Reson. Med. 83 (2020) 427–437.
[40] M. Haeberlin, L. Kasper, C. Barmet, et al., Real-time motion correction using gradient tones and head-mounted NMR field probes, Magn. Reson. Med. 74 (2015) 647–660.
[41] J. Levitt, A. van der Kouwe, J.H. Wong, L.D. Lewis, G. Bonmassar, The MotoNet: a 3 Tesla MRI-conditional EEG net with embedded motion sensors, Sensors (Basel) 23 (7) (2023) 3539.
[42] O.V. Olesen, R.R. Paulsen, L. Hojgaard, B. Roed, R. Larsen, Motion tracking for medical imaging: a nonvisible structured light tracking approach, IEEE Trans. Med. Imaging 31 (1) (2012) 79–88.
[43] D.J. Griffiths, Introduction to Electrodynamics, fourth edition, Prentice Hall, Mishawaka, USA, 1981.
[44] J.D. Jackson, Classical Electrodynamics, third edition, John Willey & Sons, Inc., New York, 1998.
[45] R. Bowtell, R.M. Bowley, Analytic calculations of the E-fields induced by time-varying magnetic fields generated by cylindrical gradient coils, Magn. Reson. Med. 44 (2000) 782–790.
[46] M. Bencsik, R. Bowtell, R.M. Bowley, Electrical fields induced in a spherical volume conductor by temporally varying magnetic field gradients, Phys. Med. Biol. 47 (4) (2002) 557–576.
[47] P.M. Glover, I. Cavin, W. Qian, R. Bowtell, P.A. Gowland, Magnetic-field-induced vertigo: a theoretical and experimental investigation, Bioelectromagnetics 28 (2007) 349–361.
[48] M. Bencsik, R. Bowtell, R.M. Bowley, Electric fields in the human body by time-varying magnetic field gradients: numerical calculations and correlation analysis, Phys. Med. Biol. 52 (2007) 1–17.
[49] E.H. Bhuiyan, Monitoring movement in MRI by measuring changes in the EMF induced in head mounted coils, Ph. D. Thesis, University of Nottingham, UK, uk.bl.ethos.728515, QC501 Electricity and magnetism, British Library, 2017.
[50] E.H. Bhuiyan, M.E.H. Chowdhury, P.M. Glover, R. Bowtell, Proc. Int. Soc. Magn. Reson. Med. 23 (2015) 1017.